A novel ductile machining model of single-crystal silicon for freeform surfaces with large azimuthal height variation by ultra-precision fly cutting

Abstract

Ultra-precision fly cutting (UPFC) is an important technology in the fabrication of freeform surfaces on single-crystal silicon. However, the insufficient understanding of the ductile machining mechanisms in UPFC of silicon under a large depth of cut highly limits the practical fabrication of freeform surfaces with large azimuthal height variation (AHV). Especially, no work has been found on studying the ductile machining model in UPFC of silicon considering both feed and step motion of the diamond tool. In this study, a novel ductile machining model in UPFC of silicon is proposed to demonstrate the superiority of UPFC on achieving the deep ductile-cut region. Experimental validation has been conducted by fabricating two kinds of freeform surfaces, namely micro-grooves and an F-theta lens, on silicon. This paper theoretically and experimentally elaborates that the chip thickness of UPFC is not only determined by the machining parameters, but also is the inversely proportional function of the swing distance of the diamond tool. Thus, by employing a large enough swing distance, much thinner chips can be generated by UPFC even when machining under large cutting depths and feed rates. Therefore, a deep ductile-cut region of silicon can be achieved by UPFC with a large swing distance. Freeform surfaces with tens of micrometers of AHV can be successfully fabricated on silicon by UPFC without the generation of brittle fractures.

Keywords: Freeform surface; Micro-groove; Single-crystal silicon; Ultra-precision fly cutting

Nomenclature		S_w	Swing distance
o-xyz	The coordinate system	S_r	Step distance
i, j, k, l, m, n		R	Tool nose radius
	The chip boundary curves	d_0	Depth of cut
h	The projecting curve of the curve *m*	f_e	Feed rate
	and *n* on the chip bottom surface	S_a,	The mean square deviation
a, b, c, d	The chip boundary points	S_t	The surface profile error
(x_0, y_0, z_0)	The point coordinate on the curve *m*	l	The distance between (x_0, y_0, z_0)
	and *n*		and (x_1, y_1, z_1)
(x_1, y_1, z_1)	The point coordinate on the curve *h*	(x_a, y_a), (x_b, y_b), (x_c, y_c)	

The coordinate of point *a*, *b* and *c*

1. Introduction

Due to its high transmission for infrared light, small thermal expansion coefficient and unique semiconducting properties, single-crystal silicon is widely applied in the infrared (IR) optical system, precision molding technology and optoelectronic industry [1, 2]. For example, diffractive structures of silicon possess excellent performance in light trapping, so this type of structures is able to be utilized to increase the trapping efficiency of solar cells [3]. Silicon based infrared optical components with spherical, aspherical or freeform shapes have been widely used in advanced IR optical systems [4]. Moreover, the advantages of silicon, such as good mechanical properties and low thermal expansion coefficient, make silicon become an important mold material in hot embossing process [5]. To fulfil requirements of precision molding, ultra-fine surface quality and high form accuracy are required for the freeform surfaces generated on silicon [6]. However, single-crystal silicon is a kind of hard-and-brittle material, which possesses very low fracture toughness and high anisotropy. These inherent defects impose great challenges in acquiring the freeform surfaces or complex microstructures featuring large azimuthal height variation (AHV) on silicon, as well as optically qualified surfaces featuring extremely low and uniform surface roughness and high form accuracy in processing silicon, whereas literature on this issue is very limited.

A variety of non-conventional fabrication technologies have been employed for the generation of complex 3D structures on silicon, such as chemical-etching and laser-assisted lithography [7, 8], with most of these technologies being based on etching mechanisms. However, the shape complexity of the generated structures by the etching processes is very limited, and it is also difficult to obtain ultra-smooth roughness with high form accuracy. According to Ottevaere et al. [9] and Harvey et al. [10], the form error and surface roughness of an optical freeform component are obligatorily restricted within the range of sub-micro scale and nano scale, respectively, to fulfil the performance of the optical components. By means of commonly adopted grinding and polishing methods, smooth spherical and aspherical surfaces have been successfully fabricated on brittle-and-hard materials like silicon [11, 12]. However, the material removal rate of these abrasive based machining methods is generally low in practical application [13].

In comparison, diamond machining technologies, dominated by fast or slow tool servos (FTS/STS)

and multi-axis diamond milling, offer a more flexible method for machining complex structures on brittle materials with a form accuracy and surface roughness corresponding to the ranges obtained via lapping and polishing [14, 15]. For example, spherical micro-lens arrays with a form error and surface roughness fulfilling IR optical performance, was machined on single-crystal silicon via STS diamond turning by Mukaida et al. [16]. In addition, Brian et al. [17] fabricated a freeform Alvarez lens with surface roughness as low as 12 nm Ra on single-crystal germanium by ductile diamond milling. However, there are two main reasons that limits the achievable AHV of the freeform surfaces generated on single-crystal silicon using diamond machining technologies: one is the hard-and-brittle nature of silicon; the other is that the substrate of an original silicon wafer is normally a perfect plane surface, which increases the necessary cutting depth when machining spherical or freeform surfaces.

Most of the ductile machining models adopted by diamond turning, FTS/STS and diamond milling are developed from the model proposed by Blake et al. [18]. In their models, the brittle material at the apex of tool tip is removed in the way of plastic deformation due to the high-pressure phase transformation (HPPT), whereas brittle fractures will take place along the tool edge where the chip thickness reaches the critical undeformed chip thickness (CUCT) [19]. Therefore, smooth surfaces can be obtained only under the two essential conditions that: subsequent tool passes remove the brittle fractures generated along the tool edge; and, no fractures propagate into the finished bottom surface. As a result, very small machining parameters, including feed rate and cutting depth, have to be carefully selected to suppress the propagating brittle fractures, which generally results in extremely low machining efficiency as well as limited AHV of the generated freeform surface. In addition, deep micro-grooves are also difficult to fabricate based on this cutting operation, as the brittle fractures inevitably occurring along the tool edge cannot be removed without subsequently feeding the diamond tool in the groove-side direction.

By means of ultra-precision fly cutting (UPFC), some scholars conducted the cutting experiments with variable depth of cut for determining critical chip thickness of brittle materials [20, 21]. For example, O'Connor et al. [20] studied the effect of crystallographic orientation on the critical chip thickness of silicon through observing the surface quality of the arc-shaped groove generated by a rotational fly-cutting tool. Similarly, Liu et al. [21] conducted fly cutting experiments on silicon to investigate the effect of cutting speed on brittle-ductile transition thickness. However, in these studies, the diamond tool rotates for one rotation without feed motion, and non-overlapping cutting trajectory is

formed. Hence, the ductile machining model in this case is similar to that of plunge cutting, where chip thickness is approximately equal to the instantaneous depth of cut. This ductile machining model is superior in investigating brittle-ductile transition mechanism, but difficult to be applied to fabricate functional surfaces on brittle materials.

Preliminarily, some scholars investigated the ductile machining mechanisms of UPFC in the grooving of brittle materials [22, 23]. R. KOMIYA et al. [22] successfully fabricated a 10 μm deep micro-groove with smooth surface quality on calcium fluoride using diamond fly cutting method. In the same way, YY. Yan et al. [24] and Y. Peng et al. [23] fabricated 4 μm deep micro-grooves on silicon. In these studies, the ductile machining capability of fly cutting is well demonstrated. However, the ductile machining models proposed in these studies only considers the feed motion of the diamond tool, so these models are only applicable to the fly-grooving of one-dimensional structures. Nevertheless, both feed motion and step motion are required for fly cutting to generate arbitrarily shaped freeform surfaces. The step motion induces a more complex 3D chip morphology that is non-symmetrical with respect to the rotation plane. However, no work has been found on studying the ductile machining model in UPFC of silicon considering both feed and step motion of the diamond tool. More importantly, the cutting depth adopted in previous studies is small (less than 10 μm), and the ductile machining mechanism of fly cutting under a large depth of cut (over tens of micrometers) has not been fully understood.

Facing the above-mentioned dilemmas, a ductile machining model in UPFC of silicon considering both feed and step motion of the diamond tool is proposed in this paper to theoretically demonstrate the superiority of fly cutting on achieving deep ductile-cut region on silicon. In addition, two kinds of widely applied freeform surfaces including micro-grooves and an F-theta lens were also fabricated to demonstrate the effectiveness of the proposed model. This research provides a comprehensive understanding of the ductile machining mechanisms of fly cutting under a large depth of cut as well as is meaningful in the manufacturing of freeform surfaces with large azimuthal height variation (AHV) on silicon or other brittle materials with optically qualified surfaces as well as high form accuracy.

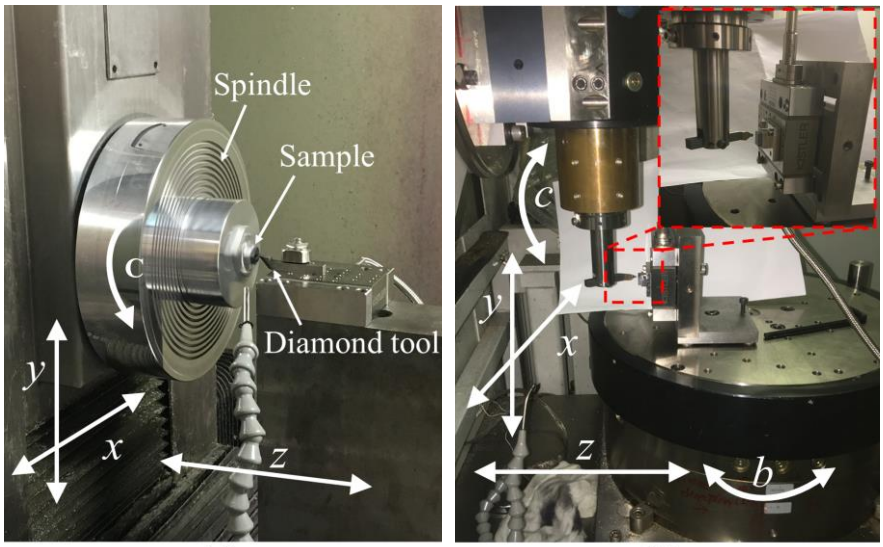

Fig. 1. Experimental setups for (a) plunge cutting and (b) UPFC.

Table 1. Cutting conditions for taper grooves.

Cutting parameteres	Plunge cutting	UPFC
Feed rate (mm/min)	none	1.8
Tilt angle (°)	0.1	0.1
Spindle rotation rate (rpm)	none	600
Cutting speed (m/s)	0.002	1.95
Swing distance (mm)	none	31.07
Cutting dirction	<110>	<110>
Cutting atmophere	Dry	Dry

2. Experimental details

Taper grooves with a tilt angle of 0.1° were machined on a p-type single-crystal silicon (001) wafer in <110> direction by plunge cutting and UPFC, respectively. For plunge cutting, the experiments were performed on a 4-axis ultra-precision lathe (Moore Nanotech 350FG, USA), as shown in Fig. 1 (a). The sample glued on the fixture was plunged by feeding the diamond tool upwards with a preset cutting speed and tilt angle, in which the depth of cut increases continuously in the *z* direction. For UPFC, the taper grooves were machined on a 5-axis ultra-precision milling machine (Precitech Freeform 705G), as shown in Fig. 1 (b). The diamond tool was fixed on the aerostatic bearing spindle and rotates with the spindle, while the workpiece was mounted on the *b*-axis. The feed motion of the spindle in UPFC machined the taper grooves. The machining parameters of the taper grooves fabricated by plunge cutting and UPFC are listed in Table 1 above.

Table 2. Cutting conditions for UPFC micro-grooves and F-theta lens.

Cutting parameteres	Micro-grooves	F-theta lens
Feed rate (mm/min)	1.8	2.7
Depth of cut (μm)	16	10
Step distance (μm)	130	10
Spindle rotation rate (rpm)	600	900
Cutting speed (m/s)	1.95	2.86
Swing distance (mm)	31.07	30.44
Cutting direction	<100>	<100>
Cutting atmophere	Dry	Dry

Freeform surfaces including micro-grooves and an F-theta lens surface were also fabricated on single-crystal silicon (001) by UPFC under the cutting conditions shown in Table 2. Horizontal cutting strategy was applied as shown in Fig. 2, whereby the diamond tool carried by the rotating spindle cuts a profile on the workpiece surface in feed direction (*x* direction), after completion of which the diamond tool moves back to the origin point of the previous cutting with a step distance moving in the step direction (*y* direction). Through periodically moving the spindle in the feed direction and step direction, the designed freeform surface can be machined on the workpiece. It is therefore found that the cutting direction in UPFC is unchanged with respect to the crystal orientation of single-crystal silicon. The tool path generation algorithm and tool edge compensation method can be seen by referring to [25].

All the experiments were conducted under dry cutting conditions. A single crystal diamond tool (Contour Fine Tooling Inc., UK) was adopted in the experiments in both plunge cutting and UPFC with a round nose radius of 0.5 mm. The rake angle and clearance angle of the diamond tool were -25^{o} and 10^{o} respectively. Optical photographs of the machined grooves and surfaces were captured by an optical microscope (BX60, Olympus corporation, Japan). Additionally, 3D surface morphologies of the machined surfaces were also measured by a 3D optical surface profiler (Zygo Corporation, USA). Chip morphology in UPFC were observed under a scanning electron microscope (SEM). The material transformation was analyzed by a LabRAM HR 800 Raman Spectrometer.

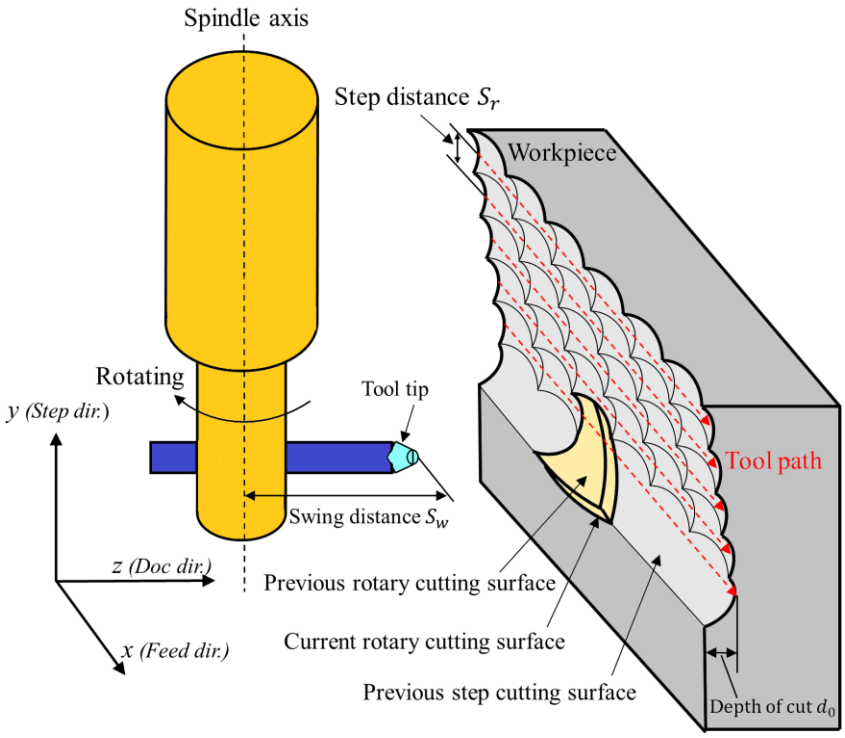

Fig. 2. Machining mechanism of UPFC.

3. Ductile machining model

For UPFC, the diamond tool feeds in the way of rotation on the silicon surface, as shown in Fig. 3, so smooth surfaces can be acquired under two specific conditions: (1) no fracture occurs during the duration of chip formation, or (2) the occasionally generated fractures along the tool path do not penetrate into the bottom surface, as these fractures will be removed by the subsequent tool rotation in the feed direction. In addition, as known from the ductile-brittle transition theory, the brittle fractures normally originate at the points where the instantaneous chip thickness reaches and exceeds the critical undeformed chip thickness (CUCT) of silicon.

Fig. 4 shows the 3D schematic morphology of the chip generated by fly cutting. For the chips generated by UPFC, thickest thickness in the step direction (TTSD) is essentially the instantaneous chip thickness, which changes from zero to its maximum value with tool rotation, as the shadow area shown in Fig. 4. During the cutting process, brittle fractures occurs on the condition that TTSD values reaches or exceeds the CUCT. Therefore, the determination of the TTSD values during the chip formation duration and comparing them with the CUCT of silicon is significant for analyzing the ductile machining model in UPFC of silicon.

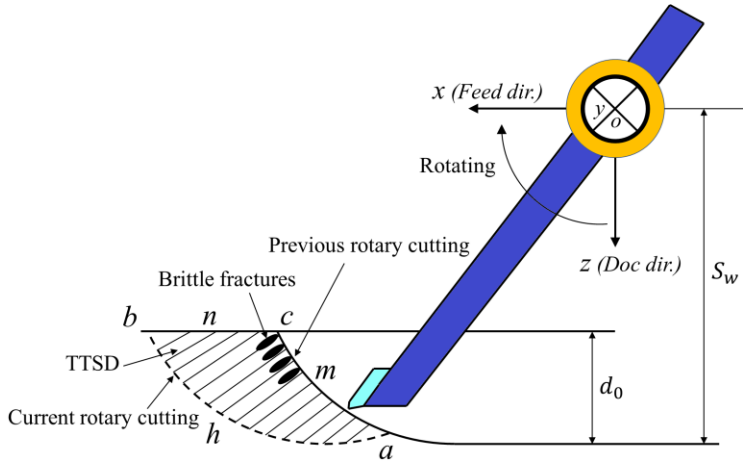

Fig. 3. Top view of UPFC process in step direction.

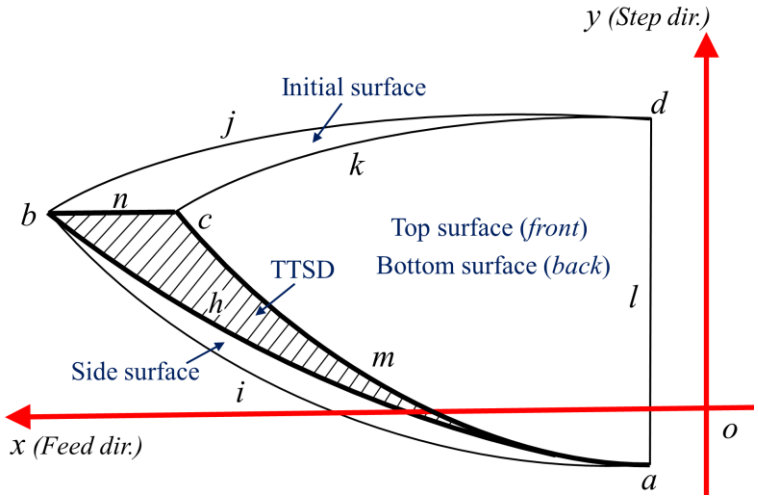

Fig. 4. Schematic chip morphology in UPFC and the TTSD.

To calculate the TTSD, a coordinate system *o-xyz* is established at the intersection point of spindle rotation axis and diamond tool holder axis, as shown in Fig. 4. Based on the geometric relation, it is found that all the TTSDs are totally distributed on the curve *n* or *m*. The TTSD values can be acquired by calculating the straight-line distance from curve *n* or *m* to the bottom surface of the chip, as the shadow area shown in Fig. 4. Furthermore, Fig. 3 illustrates the top view of UPFC in the step direction (*y* direction), with the shadow area representing TTSD. It is found that the TTSD changes as a function of tool rotation angle, which is zero at the tool-workpiece engagement and disengagement points (*a* and *b* points) and reaches its maximum value at the junction point of curve *m* and *n* (point *c*).

As the cutting duration of each tool rotation is very short, the spindle is assumed to have no movement during the chip formation in this model. The side surface, the initial surface, the bottom surface and the top surface of the diamond-milled chip can be expressed in the *o-xyz* coordinate as follows [26]:

The equation of the side surface formed by previous step cutting can be given by:

$$(z - s_w + R)^2 + (y + s_r)^2 = R^2 \tag{1}$$

where s_w is swing distance, R is the diamond tool nose radius, and s_r is the step distance. The equation of the initial surface can be obtained as:

$$z = s_w - d_0 \tag{2}$$

where d_0 is the depth of cut. The equation of the bottom surface formed by current rotary cutting can be obtained as:

$$(\sqrt{(x - f_e)^2 + z^2} - s_w + R)^2 + y^2 = R^2 \tag{3}$$

where f_e is the feed rate in mm/r. The equation of the top surface formed by previous rotary cutting is:

$$(\sqrt{x^2 + z^2} - s_w + R)^2 + y^2 = R^2 \tag{4}$$

Based on the geometrical relation described in Eq. (1), (2), (3) and (4), the shape of the chip can be mathematically described. Then, TTSD values at different distance in the feed direction can be acquired as follows.

The equations of curve *i*, *n* and *m* can be acquired by calculating the solutions of the intersecting lines formed by the corresponding two neighboring surfaces. For curve *i*, which is bounded by the side surface and bottom surface of the chip, it can be calculated by combining Eq. (1) and Eq. (3) as:

$$x = f_e + \sqrt{s_r(2y + s_r) - 2(s_w - R)(\sqrt{R^2 - (y + s_r)^2} - \sqrt{R^2 - y^2})} \tag{5}$$

Similarly, for curve *n*, which is bounded by the initial surface and the side surface, it can be obtained by combining Eq. (1) and (2), which yields:

$$y = \sqrt{d_0(2R - d_0)} - s_r \tag{6}$$

For curve *m*, which is bounded by the top surface and the side surface, it can be acquired by the same solution of Eq. (1) and Eq. (4), given as:

$$x = \sqrt{s_r(2y + s_r) - 2(s_w - R)(\sqrt{R^2 - (y + s_r)^2} - \sqrt{R^2 - y^2})} \tag{7}$$

Moreover, as shown in Fig. 3, the boundary points of curve *n* and *m* include point *a*, *b* and *c*, which can be acquired by calculating the *x*- and *y*-coordinate of the intersection point of the corresponding curves. For point *a*, which is the intersection point of curves *i* and *m*, its *x*- and *y*-coordinate (x_a, y_a) can be calculated by Eq. (5) and Eq. (7) as:

$$\begin{cases} x_a = f_e/2 \\ y_a = root\ of(\sqrt{s_r(2y+s_r) - 2(s_w - R)\left(\sqrt{R^2-(y+s_r)^2} - \sqrt{R^2-y^2}\right)} - f_e/2 \end{cases} \tag{8}$$

As the exact expression of y_a is difficult to be solved, its value can be acquired by calculating the same root of the above equation. For point *b*, which is the intersection point of curves *i* and *n*, its *x*- and *y*-coordinate (x_b, y_b) can be obtained by Eq. (5) and Eq. (6) as:

$$\begin{cases} x_b = f_e/2 + \sqrt{(\sqrt{R^2 - d_0(2R-d_0) + 2s_r\sqrt{d_0(2R-d_0)} - s_r^2} - R + s_w)^2 - (s_w - d_0)^2} \\ y_b = \sqrt{d_0(2R-d_0)} - s_r \end{cases} \tag{9}$$

For point *c*, which is the intersection point of curves *m* and *n*, its *x*- and *y*-coordinate (x_c, y_c) can be calculated by Eq. (6) and Eq. (7) as:

$$\begin{cases} x_c = \sqrt{(\sqrt{R^2 - d_0(2R-d_0) + 2s_r\sqrt{d_0(2R-d_0)} - s_r^2} - R + s_w)^2 - (s_w - d_0)^2} \\ y_c = \sqrt{d_0(2R-d_0)} - s_r \end{cases} \tag{10}$$

Assuming that the coordinate (x_0, y_0, z_0) denotes the points on curve *m* and *n*. Therefore, considering the boundary point *b* and *c*, any points (x_0, y_0, z_0) on curve *n* can be expressed as:

$$\begin{cases} x_c \le x_0 \le x_b \\ y_0 = \sqrt{d_0(2R-d_0)} - s_r \\ z_0 = s_w - d_0 \end{cases} \tag{11}$$

Similarly, considering the boundary points *a* and *c*, the points (x_0, y_0, z_0) on curve *m* can be given as:

$$\begin{cases} x_0 = \sqrt{s_r(2y_0+s_r) - 2(s_w - R)(\sqrt{R^2-(y_0+s_r)^2} - \sqrt{R^2-y_0^2})} \\ y_a \le y_0 \le y_c \\ z_0 = s_w - R + \sqrt{R^2 - (y_0+s_r)^2} \end{cases} \tag{12}$$

As discussed above, the curve *h* is the projecting line of curve *n* and *m* on the bottom surface, so the coordinate of the point on curve *h* (x_1, y_1, z_1) can be defined as the intersection point between the bottom surface and the straight line passing though the point $(f_e, 0, 0)$ and the point (x_0, y_0, z_0) on curve *m* or *n*. The equation of the line passing though the $(f_e, 0, 0)$ and (x_0, y_0, z_0) can be derived as:

$$\frac{x - f_e}{x_0 - f_e} = \frac{y}{y_0} = \frac{z}{z_0} \tag{13}$$

Based on Eq. (3) and Eq. (13), the points (x_1, y_1, z_1) on curve *h* can be expressed as:

$$\begin{cases} x_1 = K(x_0 - f_e) \\ y_1 = Ky_0 \\ z_1 = Kz_0 \end{cases} \tag{14}$$

Where:

$$K = \frac{(s_w - R)\sqrt{(x_0 - f_e)^2 + z_0^2} + \sqrt{R^2(x_0 - f_e)^2 + R^2 z_0^2 - y_0^2 s_w(s_w - 2R)}}{(x_0 - f_e)^2 + y_0^2 + z_0^2} \tag{15}$$

TTSD values is essentially the length l between the point (x_0, y_0, z_0) and the point (x_1, y_1, z_1), which yields:

$$l = \sqrt{(x_1 - x_0)^2 + (y_1 - y_0)^2 + (z_1 - z_0)^2} \tag{16}$$

As found from Eq. (12), (14), (15) and (16), TTSD is the function of both the machining parameters and the swing distance.

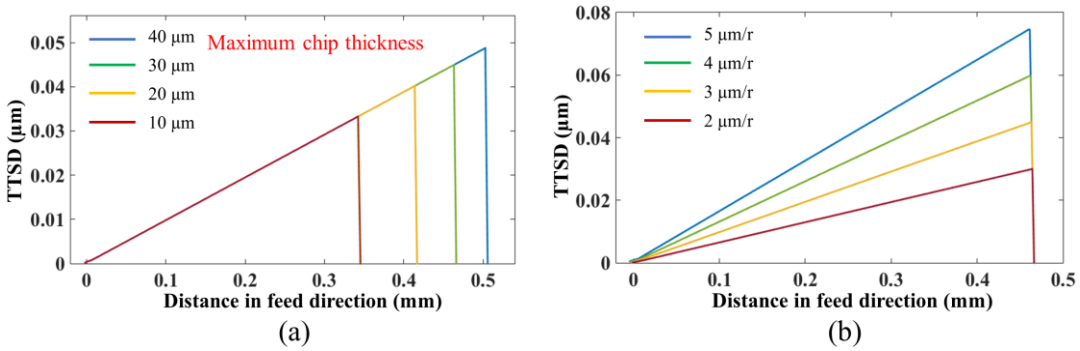

Fig. 5. Variation of the TTSD with respect to the distance in feed direction at different cutting depths and (b) feed rates.

4. Results and discussion

4.1 Ductile material removal mechanism

As found from the ductile machining model in UPFC of silicon, ductile-to-brittle transformation occurs only when the TTSD values reaches or exceeds the critical undeformed chip thickness (CUCT) of silicon. As a result, the key point in analyzing the ductile machining mechanisms of UPFC is to calculate the variation of the TTSD values with respect to the distance in the feed direction. As shown in Fig. 5, TTSD values at different cutting depths and feed rates increase gradually from zero to its maximum value, then sharply reduces to zero again. This trend is in accordance with the schematic chip morphology of UPFC, which is characterized as thicker in the center and thinner near the sides, as shown in Fig. 4. Additionally, it is learned from Fig. 5 (a) and (b) that the increasing depth of cut has no influence on the increasing rate of the chip thickness, while increasing feed rates obviously increase the increasing rate of the chip thickness with tool rotation. In other words, the machining mechanism of fly cutting is more influenced by feed rates.

As shown in Fig. 6 (a), (b) and (c), the maximum value of TTSD, representing the thickest chip thickness (TCT), increases with the increase of feed rate, depth of cut and step distance. Nevertheless, the maximum chip thickness is in the nano-scale range even under tens of micrometer cutting depth. For example, when machining with a feed rate at 3 μm/r, depth of cut at 50 μm and step distance at 10 μm, the maximum chip thickness is estimated at only ~35 nm. According to the proposed model, this thinner chip thickness compared with the preset depth of cut is mainly attributed to the rotationally cutting trajectory of the diamond tool, which makes the chip thickness of UPFC become the function of swing distance. As shown in Fig. 6 (d), the maximum chip thickness highly decreases with increasing swing distance. As a result, through adopting a large enough swing distance, very small chip thickness can be achieved by UPFC even when adopting large depth of cut in the machining process, which accordingly provides the possibility of ductile machining of silicon for freeform surfaces with large AHV.

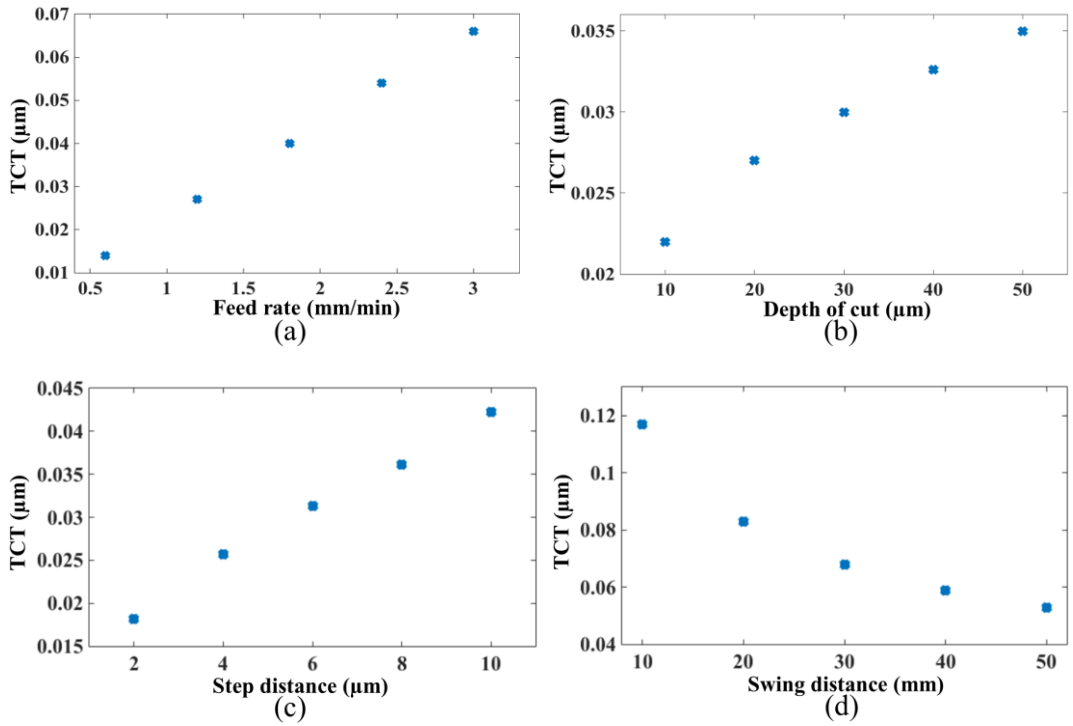

Fig. 6. The change of the TCT at different (a) feed rates, (b) cutting depths, (c) step distance and (d) swing distance.

In contrast, for the ductile machining model applied in diamond turning as well as fast or slow tool servo, the chip thickness is mainly determined by the machining parameters and tool edge radius [16, 18]. Thus, the allowable cutting depths and feed rates of diamond turning are generally very small

in machining silicon, to avoid the penetration of brittle fractures into the bottom surface, thereby limit the achievable AHV of the generated freeform surfaces.

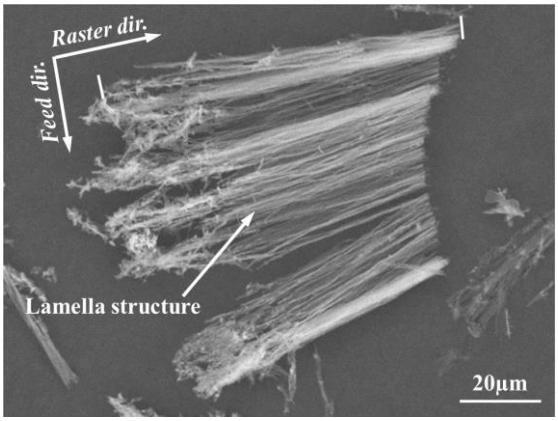

Fig. 7. SEM images of the chip morphology obtained from UPFC.

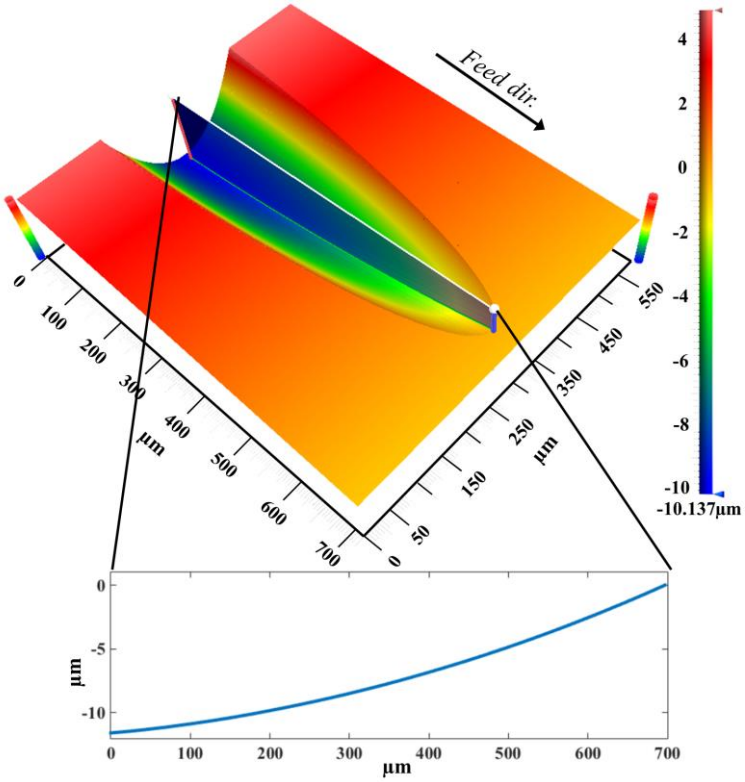

Fig. 8. 3D morphology of the tool-withdrawal-groove and its cross-profile in the groove-center along the feed direction.

Even though the calculated TCT values of UPFC increases linearly with increasing feed rate, depth of cut and step distance, as shown in Fig. 6 (a), (b) and (c), their values remain less than the CUCT of silicon which is reported in the range of 99~182 nm [27], suggesting a totally ductile material removal model in the cutting process of UPFC under relatively large feed rate and cutting depth. This

ductile material removal behavior can be validated by the integrated chip topography acquired from UPFC as shown in Fig. 7, which when compared with the schematic chip morphology as shown in Fig. 4 indicates a continuous chip formation process without brittle fracture. The lamella structures distributed on the chip suggests the plastic deformation of the silicon, instead of brittle fractures [28]. The smooth tool-withdrawal-groove surface quality, as shown in Fig. 8, acquired by the last rotational cutting trajectory in the feed direction also validates the consumption of the totally ductile material removal behavior during the whole cutting process. As shown in Fig. 9, both amorphous silicon and poly-crystalline were observed in the Raman spectrum of the cutting chips, which further validates the ductile material removal process of silicon by UPFC. Similar results were also observed by Yan et al. [29] and Mukaida et al. [16].

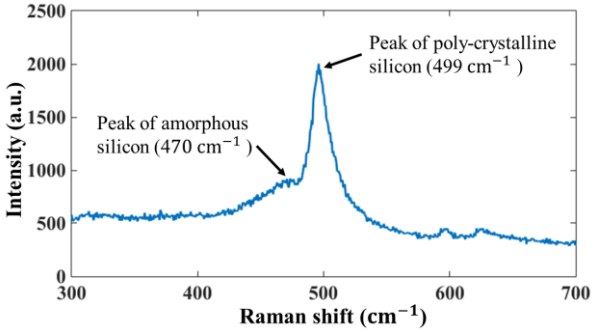

Fig. 9. Raman spectrum of the chips generated by UPFC.

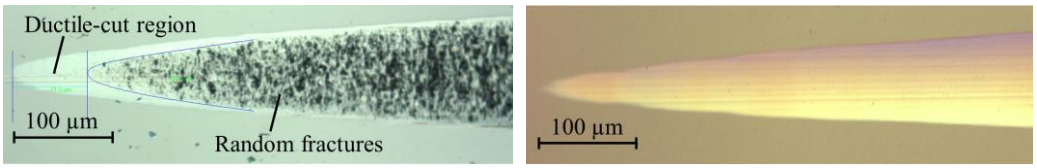

(a) (b)

Fig. 10. Optical microscopy of the taper grooves machined by (a) plunge cutting and (b) UPFC.

4.2 Micro-grooves

To further validate the proposed model, taper grooves with gradually varying depth of cut were machined on single-crystal silicon in <110> direction by plunge cutting and UPFC, respectively. Fig. 10 and Fig. 11 illustrate the optical microscopy of the taper grooves and their corresponding centerlines. For the plunge-cut groove as shown in Fig. 10 (a), the transitional boundary between the ductile-cut region and brittle-cut region can be clearly observed. The ductile-cut surfaces are as smooth as the original silicon surface, while the brittle-cut surfaces present significantly rugged appearances. In

addition, the critical unreformed chip thickness (CUCT) in <110> direction is 89 nm, which is measured at the cutting depth where the transition point between the ductile-cut and brittle-cut regions occurs, as shown in Fig. 11 (a). Only when the cutting depth is below the CUCT, is single-crystal silicon machined in the ductile mode.

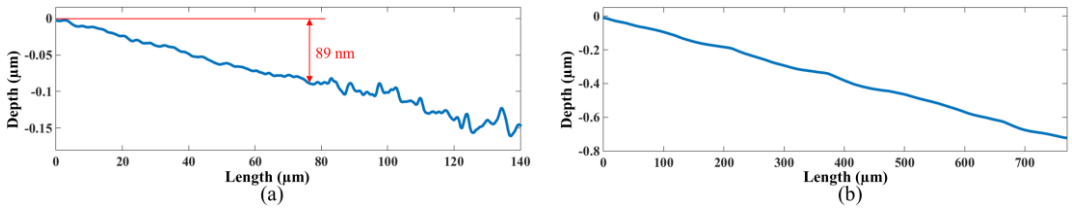

Fig. 11. Centerlines of the taper grooves machined by (a) plunge cutting and (b) UPFC.

Different from plunge cutting, the taper groove machined by UPFC presented smooth surface quality in <110> direction, as shown in Fig. 10 (b). No ductile-brittle transition can be observed indicating the totally ductile machining model of silicon by UPFC regardless of the increasing depth of cut. As shown in Fig. 11 (b), the ductile-cut region starts from the tool-workpiece engagement point to a depth of cut exceeding 700 nm, which is much larger than that machined by plunge cutting. This is because the TCT for plunge cutting is equal to the instantaneous cutting depth, so brittle fractures occur where the cutting depth reaches and exceeds the CUCT, while the TCT for UPFC is much lower than the depth of cut, as shown in Fig. 6 (b), so the material is removed in the ductile mode even though the depth of cut exceeds the CUCT. The deeper ductile-cut region of UPFC validates the proposed model and the potential of UPFC in fabricating freeform surfaces with large height difference.

Micro-grooves with depth at 16 μm were also machined by UPFC with feed rate at 1.8 mm/min and spindle speed at 600 rpm. The 3D surface morphology and the profile in the cross-sectional direction of a representative micro-groove are shown in Fig. 12 (a) and (b), respectively. It is observed that the surface quality is smooth and totally fracture-free from the groove sides to the center. Its profile in the cross-sectional direction perfectly matches the profile of the diamond tool. This validates the difference of the ductile machining process between diamond turning and UPFC. Specifically, the ductile machining mechanism of diamond turning is based on the removal of the fractures generated on the groove shoulder through the subsequent feed motion of the diamond tool in the groove-side direction [18, 30], while the rotational cutting trajectory of UPFC in the feed direction makes the chip thickness of the groove sides and groove center remain below the CUCT so that no brittle fractures

occur. The smooth surface quality can also be seen from the optical microscopic image as shown in Fig. 12 (c).

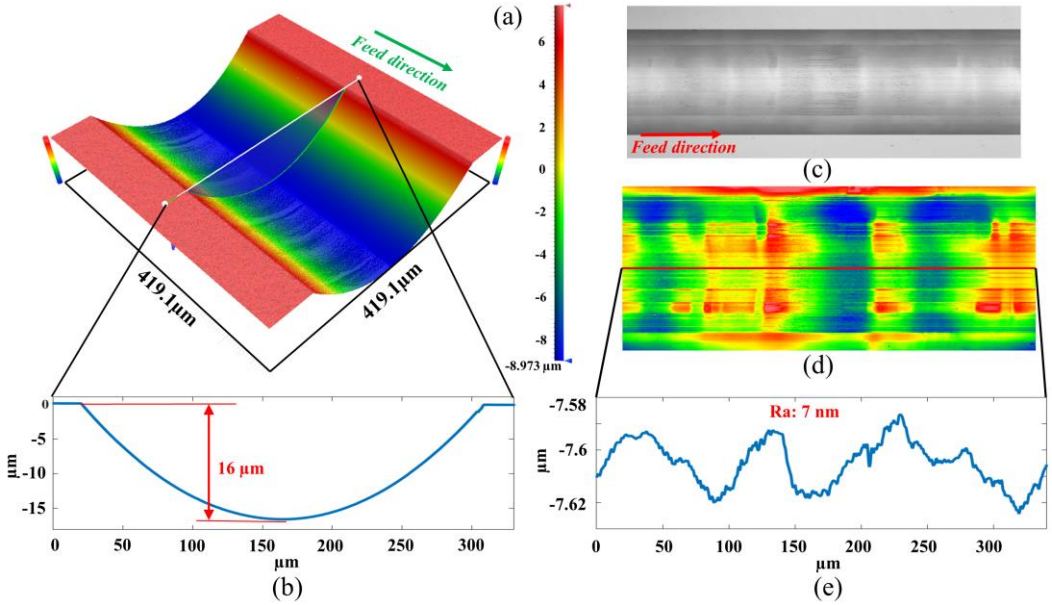

Fig. 12. Surface morphology of the micro-groove machined by UPFC in <110> direction, (a) optical 3D morphology and (b) its corresponding cross-sectional profile and (c) optical microscopic image, (d) Deviation from cylinder and (e) its profile of groove center.

Fig. 12 (d) shows the planarized micro-topography of the micro-groove surface and its central profile is shown in Fig. 12 (e). It was observed that the surface roughness measured in the groove center is 7 nm Ra and the form error is 0.041 μm PV. For an IR optical component, the required form error and surface roughness are mainly determined by the wavelength of the incident light [9, 10]. For single-crystal silicon, the wavelength of transmitting light ranges from 1.2 to 6 μm, so the form error and surface roughness of a silicon freeform optics are required to be less than 1.5 μm PV and 8 nm Ra respectively [16]. As a result, the present result has entirely satisfied the surface roughness and form accuracy requirement of the IR optical application of silicon.

As shown in Fig. 12 (d), periodic tool residual marks are distributed along feed direction, which is caused by the intermittent machining process of UPFC. The amplitude and width of these tool residual marks are entirely determined by the machining parameters and impulsive spindle vibration [31]. As shown in Fig. 13, micro-grooves with each depth at 16 μm in <110> direction were successfully fabricated on single crystal silicon. Their surface quality is similar to that of original single-crystal silicon, and on obvious fractures can be observed in the grooves. According to the proposed model, the

feasibility of UPFC in the fabrication of fracture-free micro-grooves is mainly attributed to its rotational tool trajectory in the feed direction and the large swing distance, which makes the chip thickness small enough to be machined in the ductile mode even when the depth of cut exceeds the CUCT.

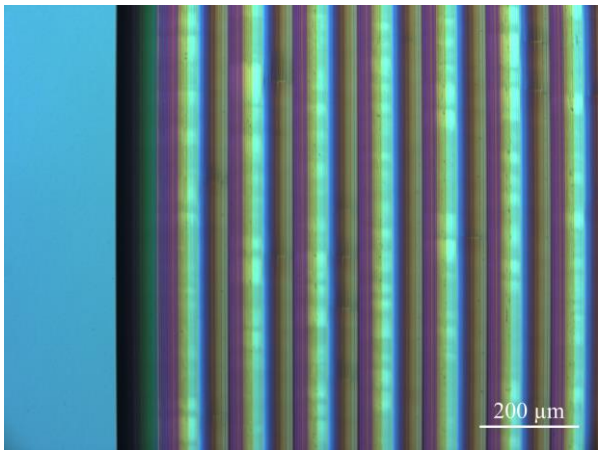

Fig. 13. Optical microscopy of the micro-grooves machined by UPFC with the depth at 16 µm.

Micro-grooves generated by previous methods, including end milling and sculpturing, are discussed for comparison. Using a force sensor integrated diamond tool, 0.1 µm deep micro-grooves were fabricated on silicon without brittle fractures [32]. With the assitance of elliptical vibration, 1 µm deep micro-grooves was generated using diamond sculpturing method [33]. Through controlling the title angle of the workpiece, 15 µm deep micro-grooves were successfully fabricated by ball end-milling method, but the surface roughness is high at 80 nm [34]. Moreover, micro-pyramid structures with a very large AHV of 200 µm were manufactured on silicon by diamond grinding, but the surface roughness and form error are also very high at 260 nm and 47.9 µm, respectively [35]. In contrast, as shown in Fig. 12, 16 µm deep micro-grooves are successfully fabricated on silicon in ductile mode by UPFC, and the surface roughness (7 nm Ra) is much lower than that acquired by end milling or grinding methods.

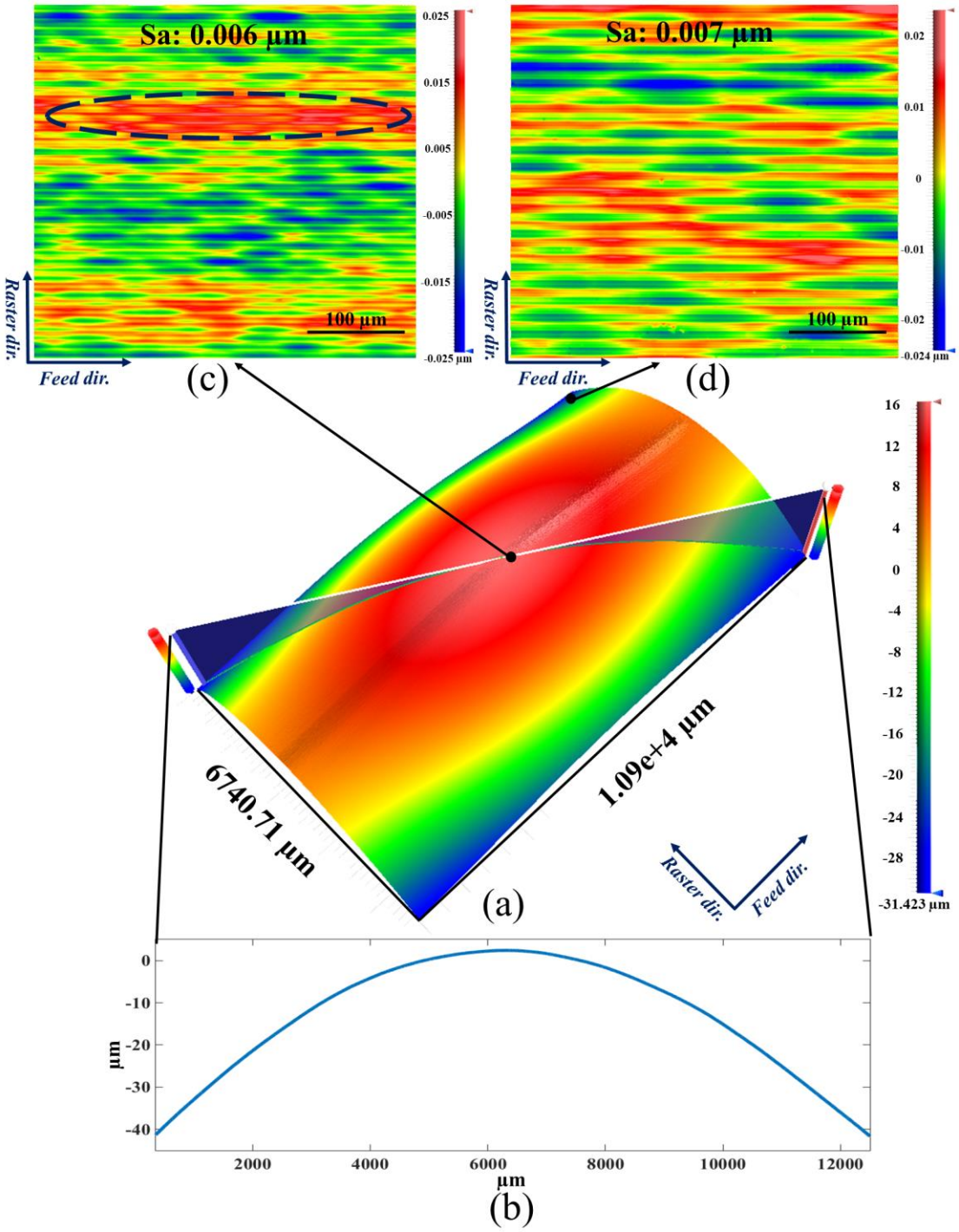

Fig. 14. Surface morphology of the F-theta lens surface machined by UPFC: (a) 3D morphology and (b) its corresponding diagonal profile and micro-topography of (c) center area and (d) marginal area.

4.3 F-theta lens surface

Apart from the micro-grooves, the proposed ductile machining model is also applicable to the fabrication of freeform surfaces on single-crystal silicon. In this research, a F-theta lens surface was directly machined on the single-crystal silicon, which can be mathematically described by $z = ax^2 +$

$bx^4 + cy^2$ with $a = -0.0007$, $b = 1.807 \times 10^{-5}$ and $c = -0.003$. Horizontal machining strategy was applied in <100> direction to avoid the influence of anisotropy of single-crystal silicon on machined surface uniformity. A polished single-crystal silicon wafer with a plane surface was used as the raw material.

Fig. 14 shows the characteristics of the fabricated F-theta lens surface measured by a 3D optical surface profiler (Zygo Corporation, USA) and its surface profile in the diagonal direction. Fig. 14 (a) illustrates the overview of the surface morphology captured and stitched by a few large areas of 1.5×1.5 mm^2. It is observed that the surface is extremely smooth without any random fractures or bulk cleavages, which indicates the dominance of ductile machining mode and no brittle fractures propagating into the finished surface. Its diagonal profile reveals that the azimuthal height variation of the F-theta lens exceeds 40 μm, as shown in Fig. 14 (b). Meanwhile, as known for ductile machining of single-crystal silicon by diamond turning or slow/fast tool servo, surface roughness changes in different crystallographic orientations and its optical micro-topography is prone to regularly repeating distribution like radial spokes [16, 36], which is mainly attributed to the high anisotropy of single-crystal silicon and the continuous change of cutting direction with respect to the crystallographic direction. In comparison, as shown in Fig. 14 (a), the overall surface presents uniform quality without any non-uniform marks induced by the anisotropy of single-crystal silicon, which is due to the unchanged cutting direction of UPFC.

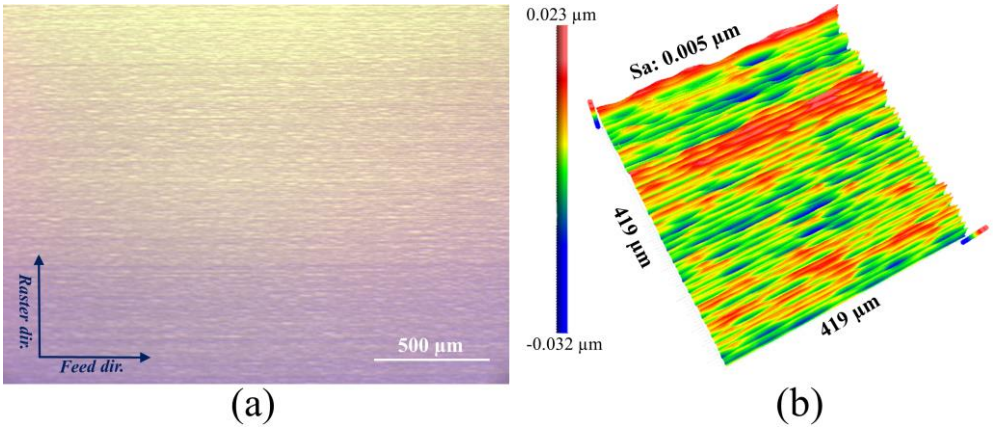

Fig. 15. (a) Optical microscopy and (b) 3D topography of the center area of the F-theta lens surface.

The micro-topography of the center area and the marginal area is compared in Fig. 14 (c) and (d), which can further illustrate the uniformity of the F-theta lens surface. The area surface roughness at the

center area is almost equal to that of the marginal area, at 6 nm Sa and 0.007 μm Sa respectively. Additionally, the micro-topography of the two areas is characterized by inhomogeneous scallops, which are induced by the intermittent cutting process. Some ribbon stripes can also be observed along the feed direction indicated by the dashed ellipse in Fig. 14 (c), which is the result from the irregular impulse spindle vibration in UPFC [37]. The inhomogeneous scallops and ribbon stripes can be clearly observed in the optical microscopic image as shown in Fig. 15, which is similar to the surface micro-topography acquired on soft and ductile materials, such as copper [31]. Despite existing ribbon stripes on the finished surface, the surface roughness is very small at 0.005 μm Sa, as shown in Fig. 15 (b).

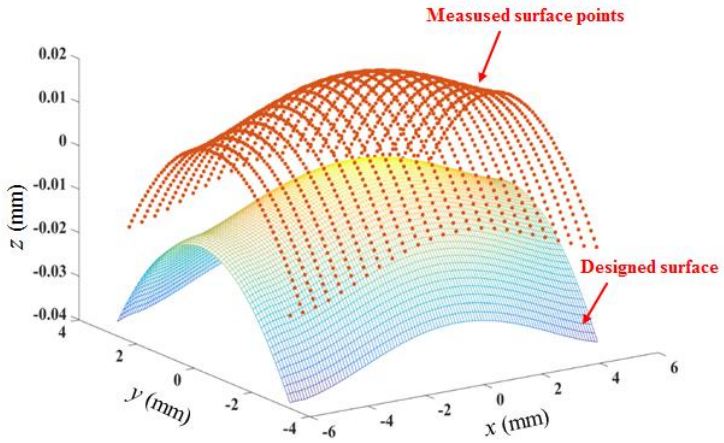

Fig. 16. Comparison between the designed surface and measured surface points.

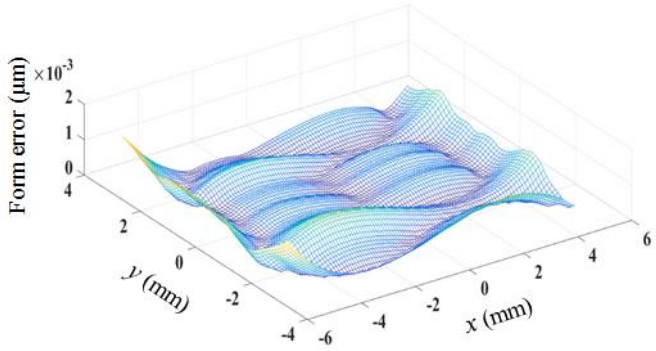

Fig. 17. Distribution of the form error.

To characterize the surface roughness and the form error of the machined surface with respect to the designed surface, the mean square deviation S_q and the surface profile error S_t is calculated below. An array of points on the F-theta lens surface was first acquired by optical surface profiler Zygo. These points were then reconstructed on the basis of iterative closest point (ICP) algorithm to minimize

the difference between two clouds of points [38], as shown in Fig. 16. After the reconstruction, the distance d_i between the measured surface point (x_i, y_i, z_i) and its corresponding designed surface point (x_i', y_i', z_i') is calculated as follows:

$$d_i = \pm\sqrt{(x_i - x_i')^2 + (y_i - y_i')^2 + (z_i - z_i')^2} \tag{16}$$

The mean square deviation S_q can be expressed as

$$S_q = \sqrt{\frac{1}{n}\sum_{i=1}^{n} d_i^2} \tag{17}$$

where n is the number of measured points. Similarly, the surface profile error S_t can be acquired by

$$S_t = |\max(d_i) - \min(d_i)| \tag{18}$$

where max() is the maximum function and min() is the minimum function. The 3D morphology of the form error represented by d_i is shown in Fig. 17. The calculated S_q and S_t is at 0.32 nm and 1.7 μm respectively. This further validates the ability of UPFC on ductile machining of freeform surfaces on single-crystal silicon with very high surface quality and low form error. Mao Mukaida and Jiwang Yan [17] discussed the general requirement of the roughness and form accuracy for a silicon optical component. They reported that the form error of a silicon IR optical component should be less than 300 nm for 1.2 μm wavelength, and 1.5 μm for 6 μm length. Besides, the roughness should be less than 8 nm Ra to fulfill IR optical application. Based on this conclusion, the surface roughness and form accuracy of the freeform surfaces generated by UPFC fulfil the IR application.

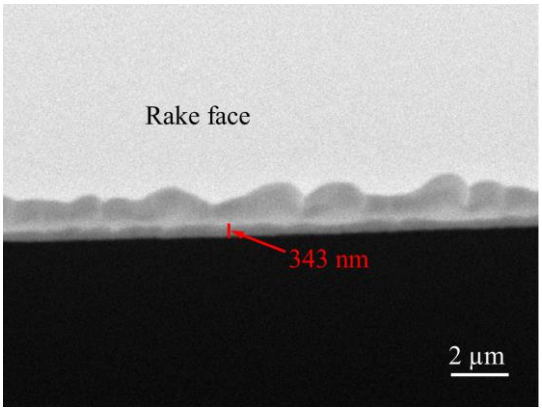

Fig. 18. SEM image of tool edge after cutting on single-crystal silicon for 200 m by UPFC.

By diamond turning using slow tool servo, sinusoidal surface with an AHV of 1 μm [39] and micro-lens arrays with an AHV of 5.5 μm [16] were successfully fabricated on silicon in ductile mode. In contrast, the AHV of the F-theta lens generated by UPFC (over 40 μm) is much larger, and its

surface roughness and the form error are only 6 nm Sa and 1.7 μm St. It is worth to note that due to the interference of the large swing distance of the diamond tool, concave freeform surfaces with small curvature radius, such as concave micro-lens arrays, are difficult to be generated by UPFC.

Fig. 18 shows the SEM image of the diamond tool after a total cutting distance of 200 m on silicon by ultra-precision fly cutting. Micro-ruggedness with a width of 343 nm can be observed on the rake face of the diamond tool. Similar tool wear patterns were also observed in diamond turning of silicon [16, 40, 41]. The micro-ruggedness mainly results from the combined effect of the high hydrostatic pressure in the cutting region as well as the periodic severe abrasive between the tool edge and the workpiece surface.

5. Conclusions

The ductile machining model in ultra-precision fly cutting (UPFC) of silicon is different from that in turning and end milling, due to its unique cutting process. However, the insufficient understanding of the ductile machining mechanisms in UPFC of silicon greatly limits the practical fabrication of freeform surfaces with large azimuthal height variations (AHV). Especially, the cutting behavior in UPFC of silicon under a large depth of cut was not yet been investigated in depth. Therefore, this paper proposes a novel ductile machining model in UPFC of silicon to discusses its ductile machining mechanisms under a large depth of cut. The theoretical and experimental study gives a better understanding of the ductile machining mechanisms in UPFC of silicon under a large depth of cut, as well as provides an effective method to fabricate freeform surfaces with large AHV on silicon so that the first findings are achieved as follows:

(1) In UPFC, the step motion of the diamond tool leads to an asymmetrical 3D chip morphology, and its thickest thickness in the step direction (TTSD) yields a crucial impact upon the brittle-ductile transition behavior of silicon.

(2) The thickest chip thickness of UPFC is the inversely proportional function of the swing distance of the diamond tool. As a result, a deep ductile-cut region of silicon can be achieved by UPFC with a large swing distance.

(3) The unchanged cutting direction in UPFC effectively reduces the adverse effects of the anisotropy of single-crystal silicon on the finished surface quality.

(4) Further, the freeform surfaces of silicon with tens of micrometers of AHV have been successfully

fabricated under a large depth of cut with nanometric surface roughness and micrometric form error. Significantly, the model can be used to fabricate freeform surfaces of other brittle materials with large AHV under a large depth of cut on.

References

[1] A.R.A. Manaf, J. Yan, Press molding of a Si–HDPE hybrid lens substrate and evaluation of its infrared optical properties, Precision Engineering, 43 (2016) 429-438.

[2] J. Eisenlohr, B.G. Lee, J. Benick, F. Feldmann, M. Drießen, N. Milenkovic, B. Bläsi, J.C. Goldschmidt, M. Hermle, Rear side sphere gratings for improved light trapping in crystalline silicon single junction and silicon-based tandem solar cells, Solar Energy Materials and Solar Cells, 142 (2015) 60-65.

[3] D. Zhou, R. Biswas, Photonic crystal enhanced light-trapping in thin film solar cells, Journal of Applied Physics, 103 (2008) 093102.

[4] M. Garín, R. Fenollosa, R. Alcubilla, L. Shi, L. Marsal, F. Meseguer, All-silicon spherical-Mie-resonator photodiode with spectral response in the infrared region, Nature communications, 5 (2014) 3440.

[5] Y. Li, D. Chen, C. Yang, Sub-microns period grating couplers fabricated by silicon mold, Optics & Laser Technology, 33 (2001) 623-626.

[6] D.-H. Choi, J.-R. Lee, N.-R. Kang, T.-J. Je, J.-Y. Kim, E.-c. Jeon, Study on ductile mode machining of single-crystal silicon by mechanical machining, International Journal of Machine Tools and Manufacture, 113 (2017) 1-9.

[7] J. Albero, L. Nieradko, C. Gorecki, H. Ottevaere, V. Gomez, H. Thienpont, J. Pietarinen, B. Päivänranta, N. Passilly, Fabrication of spherical microlenses by a combination of isotropic wet etching of silicon and molding techniques, Optics express, 17 (2009) 6283-6292.

[8] V. Tangwarodomnukun, J. Wang, C. Huang, H. Zhu, Heating and material removal process in hybrid laser-waterjet ablation of silicon substrates, International Journal of Machine Tools and Manufacture, 79 (2014) 1-16.

[9] H. Ottevaere, R. Cox, H.-P. Herzig, T. Miyashita, K. Naessens, M. Taghizadeh, R. Völkel, H. Woo, H. Thienpont, Comparing glass and plastic refractive microlenses fabricated with different technologies, Journal of Optics A: Pure and Applied Optics, 8 (2006) S407.

[10] J.E. Harvey, S. Schröder, N. Choi, A. Duparré, Total integrated scatter from surfaces with arbitrary roughness, correlation widths, and incident angles, Optical Engineering, 51 (2012) 013402-013401-013402-013411.

[11] A. Beaucamp, P. Simon, P. Charlton, C. King, A. Matsubara, K. Wegener, Brittle-ductile transition in shape adaptive grinding (SAG) of SiC aspheric optics, International Journal of Machine Tools and Manufacture, 115 (2017) 29-37.

[12] C. Wang, C. Cheung, L. Ho, M. Liu, W. Lee, A novel multi-jet polishing process and tool for high-efficiency polishing, International Journal of Machine Tools and Manufacture, 115 (2017) 60-73.

[13] B. Chen, B. Guo, Q. Zhao, An investigation into parallel and cross grinding of aspheric surface on monocrystal silicon, The International Journal of Advanced Manufacturing Technology, 80 (2015) 737-746.

[14] W. Zong, Z. Cao, C. He, C. Xue, Theoretical modelling and FE simulation on the oblique diamond turning of ZnS crystal, International Journal of Machine Tools and Manufacture, 100 (2016) 55-71.

[15] Z. Zhu, S. To, W.-L. Zhu, P. Huang, Feasibility study of the novel quasi-elliptical tool servo for vibration suppression in the turning of micro-lens arrays, International Journal of Machine Tools and Manufacture, 122 (2017) 98-105.
[16] M. Mukaida, J. Yan, Ductile machining of single-crystal silicon for microlens arrays by ultraprecision diamond turning using a slow tool servo, International Journal of Machine Tools and Manufacture, 115 (2017) 2-14.
[17] B.S. Dutterer, J.L. Lineberger, P.J. Smilie, D.S. Hildebrand, T.A. Harriman, M.A. Davies, T.J. Suleski, D.A. Lucca, Diamond milling of an Alvarez lens in germanium, Precision Engineering, 38 (2014) 398-408.
[18] P.N. Blake, R.O. Scattergood, Ductile-Regime Machining of Germanium and Silicon, Journal of the American ceramic society, 73 (1990) 949-957.
[19] S. Goel, X. Luo, A. Agrawal, R.L. Reuben, Diamond machining of silicon: A review of advances in molecular dynamics simulation, International Journal of Machine Tools and Manufacture, 88 (2015) 131-164.
[20] B.P. O'Connor, E.R. Marsh, J.A. Couey, On the effect of crystallographic orientation on ductile material removal in silicon, Precision Engineering, 29 (2005) 124-132.
[21] H. Liu, W. Xie, Y. Sun, X. Zhu, M. Wang, Investigations on brittle-ductile cutting transition and crack formation in diamond cutting of mono-crystalline silicon, The International Journal of Advanced Manufacturing Technology, 95 (2018) 317-326.
[22] R. Komiya, T. Kimura, T. Nomura, M. Kubo, J. Yan, Ultraprecision cutting of single-crystal calcium fluoride for fabricating micro flow cells, Journal of Advanced Mechanical Design, Systems, and Manufacturing, 12 (2018) JAMDSM0021-JAMDSM0021.
[23] Y. Peng, T. Jiang, K. Ehmann, Research on single-point diamond fly-grooving of brittle materials, The International Journal of Advanced Manufacturing Technology, 75 (2014) 1577-1586.
[24] Y. Yan, C. Yang, R. Wang, Research on the Shape Precison of the Micro-groove in the Silicon under Diamond Fly-cutting, in: MATEC Web of Conferences, EDP Sciences, 2016, pp. 03023.
[25] L. Kong, C. Cheung, S. To, W. Lee, An investigation into surface generation in ultra-precision raster milling, Journal of materials processing technology, 209 (2009) 4178-4185.
[26] G. Zhang, S. To, G. Xiao, Novel tool wear monitoring method in ultra-precision raster milling using cutting chips, Precision Engineering, 38 (2014) 555-560.
[27] G. Xiao, S. To, E. Jelenković, Effects of non-amorphizing hydrogen ion implantation on anisotropy in micro cutting of silicon, Journal of Materials Processing Technology, 225 (2015) 439-450.
[28] J. Yan, K. Syoji, T. Kuriyagawa, H. Suzuki, Ductile regime turning at large tool feed, Journal of Materials Processing Technology, 121 (2002) 363-372.
[29] J. Yan, T. Asami, H. Harada, T. Kuriyagawa, Fundamental investigation of subsurface damage in single crystalline silicon caused by diamond machining, Precision Engineering, 33 (2009) 378-386.
[30] D. Yu, Y. Wong, G. Hong, Ultraprecision machining of micro-structured functional surfaces on brittle materials, Journal of micromechanics and microengineering, 21 (2011) 095011.
[31] S. Zhang, S. To, A theoretical and experimental study of surface generation under spindle vibration in ultra-precision raster milling, International Journal of Machine Tools and Manufacture, 75 (2013) 36-45.
[32] Y.-L. Chen, Y. Cai, Y. Shimizu, S. Ito, W. Gao, B.-F. Ju, Ductile cutting of silicon microstructures with surface inclination measurement and compensation by using a force sensor integrated single point

diamond tool, Journal of Micromechanics and Microengineering, 26 (2015) 025002.
[33] J. Zhang, J. Zhang, T. Cui, Z. Hao, A. Al Zahrani, Sculpturing of single crystal silicon microstructures by elliptical vibration cutting, Journal of Manufacturing Processes, 29 (2017) 389-398.
[34] M. Arif, M. Rahman, W.Y. San, An experimental investigation into micro ball end-milling of silicon, Journal of Manufacturing Processes, 14 (2012) 52-61.
[35] J. Xie, Y. Zhuo, T. Tan, Experimental study on fabrication and evaluation of micro pyramid-structured silicon surface using a V-tip of diamond grinding wheel, Precision Engineering, 35 (2011) 173-182.
[36] P. Pawase, P. Brahmankar, R. Pawade, R. Balasubramanium, Analysis of machining mechanism in diamond turning of germanium lenses, Procedia Materials Science, 5 (2014) 2363-2368.
[37] S. Zhang, S. To, The effects of spindle vibration on surface generation in ultra-precision raster milling, International Journal of Machine Tools and Manufacture, 71 (2013) 52-56.
[38] P.J. Besl, N.D. McKay, A method for registration of 3-D shapes, IEEE Transactions on pattern analysis and machine intelligence, 14 (1992) 239-256.
[39] F. Fang, Y. Chen, X. Zhang, X. Hu, G. Zhang, Nanometric cutting of single crystal silicon surfaces modified by ion implantation, CIRP Annals-Manufacturing Technology, 60 (2011) 527-530.
[40] X. Li, T. He, M. Rahman, Tool wear characteristics and their effects on nanoscale ductile mode cutting of silicon wafer, Wear, 259 (2005) 1207-1214.
[41] M.S. Uddin, K. Seah, X. Li, M. Rahman, K. Liu, Effect of crystallographic orientation on wear of diamond tools for nano-scale ductile cutting of silicon, Wear, 257 (2004) 751-759.